Forcing dependence of atmospheric lapse rate changes dominates residual polar warming in solar radiation management climate scenarios.

Matthew Henry[1] and Timothy M. Merlis[2]

[1]Department of Mathematics, University of Exeter, Exeter, UK
[2]Department of Atmospheric and Oceanic Sciences, McGill University, Montreal, Quebec, Canada

Key Points:

- Idealized GCM simulations show residual polar warming when the solar constant is reduced to compensate for an increase in greenhouse gases.
- A single column model is used to decompose the total high latitude temperature change into the effects of the CO_2 increase, the insolation decrease, and the atmospheric energy transport change separately.
- This decomposition shows the importance of the bottom-heavy temperature change from the CO_2 increase in explaining the residual polar warming.

Corresponding author: Matthew Henry, m.henry@exeter.ac.uk

Abstract

Simulations of solar radiation management (SRM) geoengineering using comprehensive general circulation models (GCM) show a residual surface warming at high latitudes. Previous work attributes this to the difference in forcing structure between the increase in greenhouse gases and the decrease in insolation, but this neglects the induced reduction in atmospheric energy transport. Here we show that the difference in vertical structure of temperature change between increasing CO_2, decreasing insolation, and decreasing atmospheric energy transport is the dominant reason for the residual near-surface warming at high latitudes. A single column model (SCM) is used to decompose the high latitude temperature change, and shows the importance of the bottom-heavy temperature change from the CO_2 increase in explaining the residual polar warming. This model hierarchy invites caution when attributing high latitude surface temperature changes to the lapse rate feedback, as various forcings and nonlocal processes affect the vertical structure of temperature change differently.

Plain Language Summary

Solar radiation management (SRM) geoengineering has been proposed as a way of counteracting the warming effects of increasing greenhouse gases by reflecting solar radiation. When the carbon dioxide concentration (CO_2) is quadrupled and the solar constant is reduced in climate models to reach zero global mean surface temperature change, there is still residual warming in polar regions. Previous analyses suggested that it was caused by the latitudinal difference in forcing between the CO_2 increase and insolation reduction. This work shows the importance of the differences in vertical structure of atmospheric temperature change between the CO_2 increase and solar radiation reduction in explaining this residual polar warming. This underlines the importance of considering the vertical structure of temperature change caused by a given forcing when trying to understand what shapes the pattern of surface temperature change.

1 Introduction

Proposed solar radiation management (SRM) geoengineering schemes aim to cool the Earth to counteract the radiative forcing and warming from anthropogenic emissions. Injecting sulphate aerosols or their precursors in the stratosphere is one widely discussed SRM geoengineering technique, and climate model simulations of it have similar tropospheric temperature changes when compared with the idealization of reducing the solar constant (Kalidindi et al., 2015). The experiment G1 of the Geoengineering Model Intercomparison Project (GEOMIP) consists of reducing the solar constant to compensate for abruptly quadrupled CO_2 concentrations in fully coupled general circulation models (GCM) (Kravitz et al., 2011). In the G1 experiments, a residual polar warming occurs: the surface air temperature change is positive near the poles and slightly negative in the tropics (Stocker et al., 2013). Figure 1a and 1c show the atmospheric and surface temperature change respectively between the geoengineered G1 experiment and preindustrial control climate from five comprehensive climate models (listed in legend of figure 1c). While there is a slight surface cooling in the tropics, the high latitudes of both hemispheres have from 0.5K to 2K of residual warming. This residual polar warming has important consequences for the shift in the intertropical convergence zone (ITCZ) and changes in atmospheric energy transport in solar geoengineered climates (Russotto & Ackerman, 2018). It is also relevant to our understanding of the polar amplification of surface temperature change and vertical structure of temperature change under increased CO_2 (Manabe & Wetherald, 1975; Pithan & Mauritsen, 2014; Henry & Merlis, 2019).

This residual polar warming is commonly explained by the difference in latitudinal forcing structure between the increase in greenhouse gases and the decrease in insolation, which leads to a positive top-of-atmosphere (TOA) forcing at the poles, a neg-

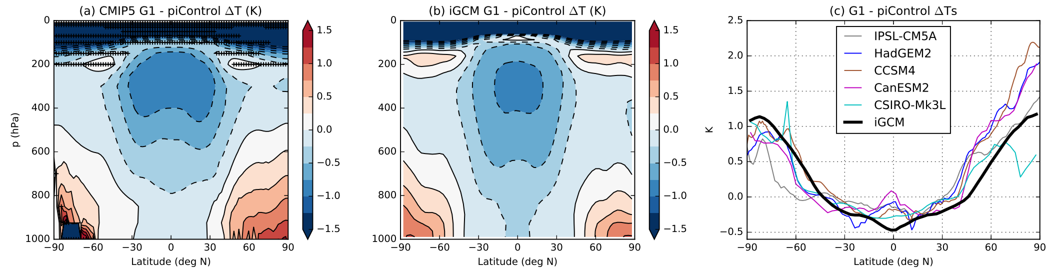

Figure 1. Residual polar warming occurs in climate model simulations of solar radiation management geoengineering. Temperature change between the solar geoengineered simulation (G1) and the preindustrial control simulation (piControl) from (a) mean of 5 CMIP5 models (IPSL CM5A, HadGEM2, CCSM4, CanESM2, CSIRO-Mk3L) and (b) idealized GCM. Crosses in (a) indicate regions where the standard deviation is larger than 1.5. (c) Surface temperature changes from the 5 CMIP5 models (colors) and the idealized GCM (black).

ative TOA forcing in the tropics, and a near-zero global-mean TOA forcing (Govindasamy & Caldeira, 2000). The tropically-amplified CO_2 forcing results from the climatological atmospheric lapse rate being larger in the tropics than near the poles (Huang et al., 2016) and is more latitudinally homogeneous than the forcing from reduced insolation (Hansen et al., 1997). This explanation, however, does not account for changes in atmospheric energy transport that result from latitudinally inhomogeneous TOA forcing. In Merlis and Henry (2018), we compute an analytic estimate of the effect of the different latitudinal structure of the solar and CO_2 forcings on the surface air temperature change in geoengineered climates that includes the effect of energy transport: we find that this effect accounts for approximately half of the total residual polar warming in the absence of regional climate feedback mechanisms.

The vertical structure of atmospheric temperature change is top-heavy in the tropics and bottom-heavy in the high latitudes (figure 1a). In the tropics, the atmosphere is close to radiative-convective equilibrium: radiative cooling is balanced by convective heating. The vertical structure of temperature is approximately determined by the moist adiabat, hence the lapse rate is uniquely a function of surface temperature and relative humidity. Therefore, the lapse rate change depends only on the surface temperature change, assuming no change in relative humidity (Xu & Emanuel, 1989). Near the poles, however, the atmosphere is close to "radiative-advective" equilibrium: warming from atmospheric energy transport is balanced by radiative cooling. Cronin and Jansen (2016) use an analytic radiative-advective model of the high latitude atmosphere to show that the lapse rate response differs depending on the nature of the forcing. In their model, a positive surface forcing (e.g., an increase in convergence of ocean heat transport or absorbed solar radiation at the surface) induces a destabilizing lapse rate change, a positive longwave radiative forcing induces a more destabilizing lapse rate change than the surface forcing, and an increase in atmospheric energy transport and/or solar atmospheric heating induces a weakly stabilizing or neutral lapse rate change. Moreover, they suggested that each additional feedback such as water vapor, clouds, or surface albedo would induce a different lapse rate response. While this simple model lead to the important insight that the high-latitude lapse rate change is forcing-dependent, the simple treatment of atmospheric energy transport results in a vertically uniform temperature change. However, atmospheric energy transport convergence has been suggested to preferentially affect the mid-troposphere in high latitudes in comprehensive climate models (Laliberté & Kushner, 2013). For SRM perturbations, we expect the CO_2 forcing to have a more bottom-heavy temperature response than the reductions in solar forcing and atmospheric energy transport, leading to a high surface temperature response for a small total forcing. In this paper, we quantify the contributions of forcings and feedbacks to the total high latitude lapse rate change and concommitant surface temperature change in the solar radiation management experiment.

2 Idealized GCM experiment

We implement a SRM experiment using an idealized atmospheric GCM. A version of the Geophysical Fluid Dynamics Laboratory (GFDL) atmospheric GCM is used with no clouds, comprehensive clear-sky radiation, annual-mean insolation, and aquaplanet surface boundary conditions with no sea ice. This setup is similar to Merlis, Schneider, Bordoni, and Eisenman (2013) and to the Model of an Idealized Moist Atmosphere (MiMA) (Jucker & Gerber, 2017). In order to compensate for the cooling radiative effect of clouds, the surface albedo is set to be an approximation of Earth's TOA albedo (figure S1) instead of prescribing an idealized cloud distribution (Merlis et al., 2013) or uniformly increasing the surface albedo (Jucker & Gerber, 2017). The control simulation has a CO_2 concentration of 300 ppm and the solar constant is 1365 $\mathrm{W\,m^{-2}}$. The solar constant in the SRM run is decreased to 1317 $\mathrm{W\,m^{-2}}$ (a 3.5% reduction) in order to get zero-mean surface air temperature change when the CO_2 concentration is quadrupled. Figure S2a shows the atmospheric temperature for the control simulation and it compares well with Earth's climate.

The surface boundary condition of the idealized atmospheric GCM is an aquaplanet with a slab mixed layer ocean with the heat capacity of 1m of water and no representation of ocean heat transport. The GCM's spectral dynamical core has T42 spectral truncation for a nominal horizontal resolution of 2.8° x 2.8° and 30 vertical levels. The skin temperature is interactively computed using the surface radiative and turbulent fluxes, which are determined by bulk aerodynamic formulae. A k-profile scheme with a dynamically determined boundary layer height is used to parametrize the boundary layer turbulence. The GCM uses a simplified Betts-Miller convection scheme (Frierson, 2007). The large scale condensation is parameterized such that the relative humidity does not exceed one and the condensed water is assumed to immediately return to the surface. The model uses the comprehensive radiation scheme described in Anderson et al. (2004) (Anderson et al., 2004) with annual mean insolation and a solar constant equal to 1365 $\mathrm{W\,m^{-2}}$. The surface has no representation of sea ice other than the surface albedo distribution, hence there is no surface albedo feedback. All simulations are run for 6000 days with time averages over the last 3000 days shown, when all climate states have reached a statistical steady state.

We perform four simulations. The control simulation has 300 ppm of CO_2 and a 1365 $\mathrm{W\,m^{-2}}$ solar constant. The increased CO_2 simulation has 1200 ppm of CO_2. The reduced solar constant experiment has a 1317 $\mathrm{W\,m^{-2}}$ solar constant. The solar radiation management experiment has both increased CO_2 and a reduced solar constant. The value for the reduced solar constant was determined in order to get near-zero global surface air temperature change. Figure S2b shows the temperature difference between the control and increased CO_2 simulation and figure S2c shows the temperature difference between the control and decreased solar constant simulation. Theres a 10% deviation from linear superposition when compared to the solar radiation management experiment's temperature change, without a significant effect on the pattern of surface temperature change.

Figure 1b shows the atmospheric temperature change between the control and SRM idealized GCM simulations, which has a similar structure to that of comprehensive GCMs (figure 1a). The surface temperature change between the control and SRM run in the idealized GCM (black) is also reasonably close to the comprehensive GCMs (figure 1c). In addition, the change in atmospheric energy transport is similar to that of comprehensive GCMs (a reduction of 0.1 PW in midlatitudes, figure S3b and figure 1 of Russotto and Ackerman (2018)). This model's ability to reproduce the temperature and atmospheric energy transport changes from comprehensive GCM simulations suggest that processes present in this idealized model are sufficient to explain the ensemble-mean changes in SRM experiments. The idealized GCM underestimates the Arctic surface temperature change from comprehensive GCMs, which is consistent with the absence of sea ice albedo feedback in the idealized GCM. We proceed to decompose the high-latitude temperature response in this GCM to identify the mechanism responsible for residual polar warming.

3 Single column model experiments

To decompose the high-latitude temperature change in the idealized GCM simulation, we use the single column model (SCM) from the ClimLab python package for process-oriented climate modeling (Rose, 2018) to emulate the high latitude troposphere of the idealized GCM. The temperature tendency budgets for atmospheric and surface temperature are given by the following equations:

$$\frac{\partial T_a(p)}{\partial t} = \frac{\partial T_a(p)}{\partial t}\bigg|_{rad} + \frac{\partial T_a(p)}{\partial t}\bigg|_{adv} + \frac{\partial T_a(p)}{\partial t}\bigg|_{cond} \tag{1}$$

$$\frac{\partial T_s}{\partial t} = \frac{\partial T_s}{\partial t}\bigg|_{rad} + \frac{\partial T_s}{\partial t}\bigg|_{SH} + \frac{\partial T_s}{\partial t}\bigg|_{LH}, \tag{2}$$

where t is time and p is pressure (with 40 pressure levels). The subscripts 'rad', 'conv', 'adv', and 'cond', 'SH', 'LH' refer to radiative, convective, advective, condensation, sensible heat flux, and latent heat flux temperature tendencies, respectively. The radiative, convective, sensible heat flux, and latent heat flux temperature tendencies are computed interactively. The RRTMG radiation scheme is used for the computation of shortwave and longwave radiative temperature tendencies. The surface albedo and control insolation are set such that the upwelling and downwelling TOA shortwave radiation match the idealized GCM simulation poleward of 80°. The horizontal atmospheric energy transport induces a temperature structure stable to convection, so including a convection parametrization has no effect. The surface sensible and latent heat fluxes are computed using bulk aerodynamic formulae with 5×10^{-2} drag coefficient and 5 ms^{-1} near surface wind speed (Rose, 2018).

Values from the idealized GCM experiments averaged poleward of 80°N are used to prescribe the specific humidity profile, which affects the radiation and surface latent heat flux. In addition, the time-mean advection and condensation temperature tendency profiles from the idealized GCM simulations are added as external temperature tendency terms to simulate the dry and moist components of atmospheric energy transport convergence, respectively. The advective temperature tendency term is calculated in the GCM as the difference in temperature tendency before and after running the dynamics module, and it, therefore, contains both the horizontal and vertical advection temperature tendencies. Because we prescribe atmospheric energy transport to the column model, we consider it to be a "forcing" in this context.

The climatological temperature profiles of the idealized GCM and SCM are similar (figure S4), though the SCM has an overly strong near-surface temperature inversion compared to the GCM. This may be due to the absence of boundary layer scheme in the SCM, which would smooth differences between the surface and lower atmospheric layers. Similarities between the temperature profiles simulated by the idealized GCM and by the SCM still hold when the latitudinal bounds of the high latitudes is set to 60° (see supplementary figure S5).

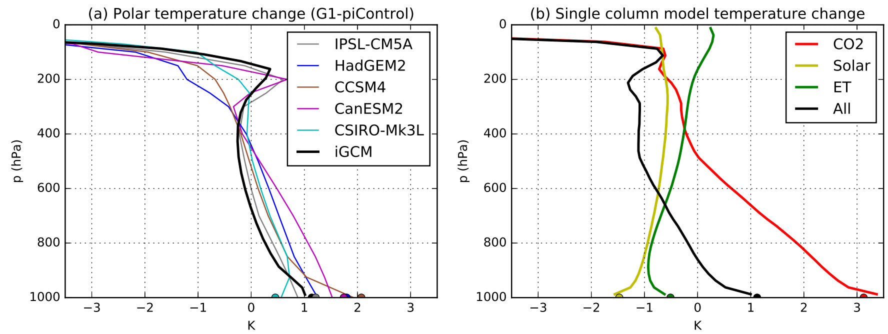

Figure 2. Residual warming arises from bottom-heavy CO_2 warming, while solar forcing and atmospheric energy transport changes have more uniform cooling. (a) Temperature difference between solar geoengineered simulation (G1) and control simulation (piControl) in the Arctic (>80° North) for the idealized GCM (black) and comprehensive GCMs (colors, listed in legend). (b) Decomposition of polar temperature change using the single column model: increased CO_2 (red), reduced insolation (yellow), decreased energy transport (green), and all perturbations (black).

We run four simulations: quadrupled CO_2, reduced insolation, perturbed energy transport, and a simulation with all perturbations (4xCO_2 and reduced insolation, energy transport, and specific humidity). A summary of the specific parameter settings for each run are given in the supplementary table S1. The separation of individual perturbations in the SCM assumes the full response to SRM is comprised of the linear superposition of these changes. Superposition holds precisely in the SCM, and largely in the idealized GCM, except for a $\approx 10\%$ difference in the global mean (figure S2).

Figure 2a shows that the idealized GCM's vertical temperature change structure in high latitudes (black, "iGCM") is similar to that of five CMIP5 models in the Arctic (colors, listed in legend). Figure 2b shows the temperature change structure for the different SCM simulations, with points showing surface (or skin) temperature changes. The CO_2-only simulation ("CO_2", red) has a bottom-heavy temperature change structure and a surface temperature increase of 3.1K. The insolation reduction simulation ("Solar", yellow) has a more vertically uniform cooling structure and a surface temperature change of -1.5K. The energy transport change ("ET", green) preferentially cools the lower atmosphere and leads to a -0.5K surface temperature change. Finally, when all perturbations (CO_2, insolation, water vapor and energy transport) are included ("All", black), the surface temperature change is 1.1K, as was simulated by the idealized GCM (1.1K). The differences between the comprehensive GCMs (figure 2a, colors), the idealized GCM (figure 2a, black), and the SCM (figure 2b, black) can be due to the different radiation schemes, to the time-averaging of boundary conditions in the SCM, and to the absence of climate components such as clouds, sea ice, and ocean circulation.

We calculate the forcing on the high latitude atmospheric column for each simulation by calculating the change in outgoing longwave radiation (OLR) induced by the changes in surface and tropospheric temperature (here, the tropopause is set at 200 hPa). The temperature kernel of the column model is calculated by separately increasing the surface and each pressure level by 1K and calculating the resulting OLR increase (see supplementary figure S7 for kernel structure). The total feedback determines the surface temperature change per unit of forcing and is decomposed into the Planck, lapse rate, and water vapor feedbacks. The change in water vapor is small and induces a negligible change in surface temperature, so it is omitted here (see supplementary figure S8). The Planck feedback is computed as the OLR change from a 1K temperature increase

Run name	ΔT_S (K)	Forcing ($\mathrm{W\,m^{-2}}$)	Lapse rate feedback ($\mathrm{W\,m^{-2}\,K^{-1}}$)
'4xCO_2'	3.1	5.1	0.79
'Solar'	-1.5	-3.0	0.43
'ET'	-0.51	-1.4	-0.20
'All'	1.1	0.63	1.9

Table 1. Values for ΔT_S, forcing and lapse rate feedback for each temperature change structure of the single column model of the polar atmosphere (figure 2b).

at the surface and in the troposphere. Its value is -2.6 $\mathrm{W\,m^{-2}\,K^{-1}}$, which is comparable to comprehensive GCM estimates in high latitudes (Feldl & Bordoni, 2016). The temperature feedback is computed as the OLR increase induced by the surface and tropospheric temperature change divided by the surface temperature change, and the lapse rate feedback as the temperature feedback minus the Planck feedback. The lapse rate feedback of the "All" experiment is 1.9 $\mathrm{W\,m^{-2}\,K^{-1}}$, which is comparable to the high latitude lapse rate feedback of the idealized GCM SRM experiment computed using aquaplanet temperature kernels (Feldl et al., 2017) (not shown).

The forcing and lapse rate feedback associated with each simulation are shown in table 1. There is a 2.1 $\mathrm{W\,m^{-2}}$ positive TOA forcing from the difference between the CO_2 and solar forcings, and a -1.4 $\mathrm{W\,m^{-2}}$ reduction in atmospheric energy transport convergence (comparable to the change in high latitude convergence of atmospheric energy transport in the idealized GCM). The relatively large surface temperature response in the "All" experiment (1.1K) for a small forcing (0.63 $\mathrm{W\,m^{-2}}$ if the change in atmospheric energy transport is considered as a forcing on the high latitude column) can be attributed to the very destabilizing lapse rate feedback (1.9 $\mathrm{W\,m^{-2}\,K^{-1}}$). If we use the lapse rate feedback of the CO_2-only simulation (0.79 $\mathrm{W\,m^{-2}\,K^{-1}}$), then the surface temperature change would be 0.4K instead of 1.1K. We are thus left with explaining this very destabilizing lapse rate feedback that provokes most of the residual polar warming in SRM simulations.

As shown in figure 2b, the vertical structure of temperature change in the "All" experiment can be decomposed into the effect of individual forcings and feedbacks. The warming from the increase in CO_2 is very bottom-heavy (0.79 $\mathrm{W\,m^{-2}\,K^{-1}}$ lapse rate feedback), whereas the cooling from changes in insolation and energy transport are more vertically homogeneous. When this vertically homogeneous cooling is superimposed on the bottom-heavy warming from CO_2, it decreases the OLR faster than it decreases the surface temperature. The vertical gradient in temperature is almost left unchanged (compare "CO_2" and "All" in figure 2b), the forcing on the atmospheric column is small, and the surface temperature change is 1.1K. Given the importance of the lapse rate changes between forcing agents, we turn to a more idealized SCM to develop a theoretical understanding of forcing dependence of high latitude lapse rate response.

4 Simplified analytical model

The analytical model of the high latitude atmosphere in radiative-advective equilibrium (Cronin & Jansen, 2016) was used to show the forcing dependence of high latitude lapse rate changes. In their model, an increase in greenhouse gases leads to a more bottom-heavy temperature change than an increase in atmospheric or surface forcing. Details including the climatological temperature and temperature changes of the analytical radiative-advective model are reproduced from Cronin and Jansen (2016) in the supplementary text S1.

The essence of the mechanism for the forcing dependence of the high latitude lapse rate change is contained in the radiative equilibrium limit (no advection) of the Cronin and Jansen (2016) (Cronin & Jansen, 2016) model, so we discuss this simpler case. We impose the convergence of atmospheric energy transport at the surface to keep the temperatures of this pure radiative equilibrium model similar to high latitudes. The parameters are $F_S = 120\ \mathrm{W\,m^{-2}}$ and $\tau_0 = 3$, where F_S is the surface forcing and τ_0 the total longwave optical depth. To further simplify the calculations, we do not include an atmospheric window and the optical depth decays as the square of the pressure normalized by the surface pressure.

It is well understood that an atmosphere in pure radiative equilibrium is statically unstable, however the argument for the perturbation temperature is fundamentally the same as for an atmosphere in radiative-advective equilibrium and easier to understand. In this model, increasing the total longwave optical depth is analogous to increasing atmospheric CO_2, and decreasing the surface forcing is analogous to decreasing the TOA insolation (atmospheric absorption of solar radiation is ignored).

Figure 3a shows the temperature change from increasing the total longwave optical depth (red) and from decreasing the surface forcing (yellow). The total longwave optical depth is increased from 3 to 3.2 and induces an instantaneous reduction in OLR by $3.6\ \mathrm{W\,m^{-2}}$, which we use for the magnitude of the reduction in surface forcing. The vertical structure of temperature change is more bottom-heavy for an increase in longwave optical depth ("CO_2", red) than for a decrease in surface forcing ("Solar", yellow). The forcing dependence of the lapse rate feedback thus does not depend on the presence of atmospheric energy transport convergence.

To explain this forcing dependence, we derive a simple expression for the temperature structure of the polar troposphere from the two-stream Schwartzchild equations for gray radiative transfer (equations 1 and 2 in supplementary text S1) with the simplifications described above:

$$2\sigma T(p)^4 = F_S[1+\tau(p)] = F_S\left[1+\tau_0\left(\frac{p}{p_0}\right)^2\right], \tag{3}$$

where F_S is the surface forcing, τ_0 the total longwave optical depth, p the pressure and p_0 the surface pressure. This equation shows that temperatures must change at all levels for a change in F_S, but they do not change as p goes to zero for a change in τ_0.

Figure 3b shows the difference in $2\sigma T^4$ from changes in τ_0 and F_S. When τ_0 is increased from 3 to 3.2, the change in $2\sigma T^4$ is zero at the TOA and $\delta\tau_0 F_S$ at the surface. When F_S is reduced from $120\ \mathrm{W\,m^{-2}}$ to $116.4\ \mathrm{W\,m^{-2}}$, the change in $2\sigma T^4$ is δF_S at the TOA and $\delta F_S(1+\tau_0)$ at the surface. Physically, an increase in greenhouse gases corresponds to a deepening of the atmosphere with respect to optical depth and the net upwards longwave radiative flux at the TOA between two equilibrium states is not affected; whereas a change in insolation affects the longwave radiative flux from the surface to the TOA. This reasoning applies for an atmosphere in pure radiative equilibrium, as well as an atmosphere in radiative-advective equilibrium (see figure S9 for an analog of figure 3 for an atmosphere in radiative-advective equilibrium).

5 Conclusion

In climate model simulations of solar radiation management (SRM) scenarios, where the solar constant is reduced to compensate for an increase in CO_2, there is residual warming in polar regions. We decompose the contributions of the CO_2 increase, insolation de-

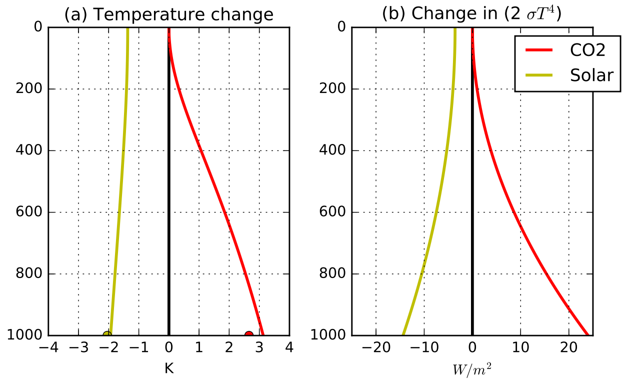

Figure 3. A pure radiative version of an analytical model of the high-latitude atmosphere (Cronin & Jansen, 2016) captures the forcing dependence of lapse rate changes. (a) Temperature change from increasing the total longwave optical depth by 0.2 (‘CO_2’, red) and from decreasing the surface forcing by 3.6 $\mathrm{W\,m^{-2}}$ (‘Solar’, yellow), which is equal to the instantaneous reduction in outgoing longwave radiation from increasing the total longwave optical depth by 0.2. (b) Change in $2\sigma T^4$, which satisfies the radiative transfer equation [3], for both perturbation experiments.

crease, and energy transport change to the vertical structure of high latitude temperature change, to understand why this residual polar warming occurs. The high latitudes are close to radiative-advective equilibrium: the cooling from radiation is balanced by warming from atmospheric energy transport convergence. Where there is convection, the temperature of the atmospheric column can be approximated based on the surface temperature and relative humidity. Without convection, each forcing and feedback induces a different lapse rate response. In the SRM experiment, the latitudinal structure of the forcing is such that the high latitudes have a positive TOA radiative forcing and a reduction in atmospheric energy transport convergence. If we consider the atmospheric energy transport convergence as a forcing on the high latitude column, then the positive TOA forcing and reduction in atmospheric transport convergence add up to give a small forcing. However, the surface temperature change is relatively large, which is explained by a destabilizing lapse rate feedback. The vertical structure of the high latitude temperature change of an idealized GCM is decomposed using a SCM. It is shown that the warming from CO_2 alone is very bottom-heavy whereas the cooling from a reduction in insolation and atmospheric energy transport are more vertically homogeneous. The combination of a bottom-heavy warming and a vertically homogeneous cooling gives a small forcing for a relatively large surface warming. Using the no advection limit of an analytical model of the high latitude atmosphere in radiative-advective equilibrium (Cronin & Jansen, 2016), we show that the difference in the vertical structure of temperature changes from increasing CO_2 and decreasing insolation result from different changes in the boundary conditions of the radiative flux. The increase in CO_2 deepens the atmosphere with respect to optical depth, whereas the change in insolation modifies the resulting longwave radiative fluxes through the whole atmosphere (surface to TOA). The dominance of the forcing agent dependence of lapse rate changes in provoking residual polar warming in SRM simulations can be assessed by replacing the lapse rate feedback with that of CO_2 (table 1) or considering models without this feedback (Merlis & Henry, 2018), both of which substantially underestimate the polar warming. An implication of the lapse rate dependence on forcing agent is that there will be residual polar surface warming even if the spatial distribution of scattering aerosols can be optimized to perfectly offset the local greenhouse gas forcing.

Data availability statement

Datasets and code for this research are available at https://github.com/matthewjhenry/HM19_SRM/ (?, ?).

Acknowledgments
This work was supported by Fonds de Recherche du Québec — Nature et Technologies (FRQNT) Nouveau Chercheur award, a Natural Sciences and Research Council (NSERC) Discovery grant, and a Compute Canada allocation. We acknowledge Brian Rose's help in setting up the single column model by adding an external forcing term.

References

Anderson, J. L., Balaji, V., Broccoli, A. J., Cooke, W. F., Delworth, T. L., Dixon, K. W., … others (2004). The new GFDL global atmosphere and land model am2–lm2: Evaluation with prescribed sst simulations. *Journal of Climate*, *17*(24), 4641–4673.

Cronin, T. W., & Jansen, M. F. (2016). Analytic radiative-advective equilibrium as a model for high-latitude climate. *Geophysical Research Letters*, *43*(1), 449–457.

Feldl, N., & Bordoni, S. (2016). Characterizing the Hadley circulation response through regional climate feedbacks. *J. Climate*, *29*(2), 613–622.

Feldl, N., Bordoni, S., & Merlis, T. M. (2017). Coupled high-latitude climate feedbacks and their impact on atmospheric heat transport. *Journal of Climate*, *30*(1), 189–201.

Frierson, D. M. (2007). The dynamics of idealized convection schemes and their effect on the zonally averaged tropical circulation. *J. Atmos. Sci.*, *64*(6), 1959–1976.

Govindasamy, B., & Caldeira, K. (2000). Geoengineering Earth's radiation balance to mitigate CO_2-induced climate change. *Geophys. Res. Lett.*, *27*, 2141–2144.

Hansen, J., Sato, M., & Ruedy, R. (1997). Radiative forcing and climate response. *Journal of Geophysical Research: Atmospheres*, *102*(D6), 6831–6864.

Henry, M., & Merlis, T. M. (2019). The role of the nonlinearity of the stefan–boltzmann law on the structure of radiatively forced temperature change. *Journal of Climate*, *32*(2), 335–348.

Huang, Y., Tan, X., & Xia, Y. (2016). Inhomogeneous radiative forcing of homogeneous greenhouse gases. *J. Geophys. Res.: Atmospheres*, *121*(6), 2780–2789.

Jucker, M., & Gerber, E. (2017). Untangling the annual cycle of the tropical tropopause layer with an idealized moist model. *Journal of Climate*, *30*(18), 7339–7358.

Kalidindi, S., Bala, G., Modak, A., & Caldeira, K. (2015). Modeling of solar radiation management: a comparison of simulations using reduced solar constant and stratospheric sulphate aerosols. *Climate Dynamics*, *44*(9-10), 2909–2925.

Kravitz, B., Robock, A., Boucher, O., Schmidt, H., Taylor, K. E., Stenchikov, G., & Schulz, M. (2011). The geoengineering model intercomparison project (GeoMIP). *Atmospheric Science Letters*, *12*(2), 162–167.

Laliberté, F., & Kushner, P. (2013). Isentropic constraints by midlatitude surface warming on the Arctic midtroposphere. *Geophysical Research Letters*, *40*(3), 606–611.

Manabe, S., & Wetherald, R. T. (1975). The effects of doubling the CO_2 concentration on the climate of a general circulation model. *J. Atmos. Sci.*, *32*, 3–15.

Merlis, T. M., & Henry, M. (2018). Simple estimates of polar amplification in moist diffusive energy balance models. *Journal of Climate*(2018).

Merlis, T. M., Schneider, T., Bordoni, S., & Eisenman, I. (2013). Hadley circulation response to orbital precession. Part I: Aquaplanets. *J. Climate*, *26*, 740–753.

Pithan, F., & Mauritsen, T. (2014). Arctic amplification dominated by temperature feedbacks in contemporary climate models. *Nat. Geosci.*, *7*, 181–184.

Rose, B. E. (2018). Climlab: A python toolkit for interactive, processoriented climate modeling. *J. Open Source Software*, *3*(24), 659.

Russotto, R. D., & Ackerman, T. P. (2018). Energy transport, polar amplification, and ITCZ shifts in the GeoMIP G1 ensemble. *Atmospheric Chemistry and Physics*, *18*(3), 2287–2305.

Stocker, T. F., et al. (Eds.). (2013). *Climate change 2013: The physical science basis.* Cambridge and New York: Cambridge University Press.

Xu, K.-M., & Emanuel, K. A. (1989). Is the tropical atmosphere conditionally unstable? *Monthly Weather Review*, *117*(7), 1471–1479.

fig1.eps.

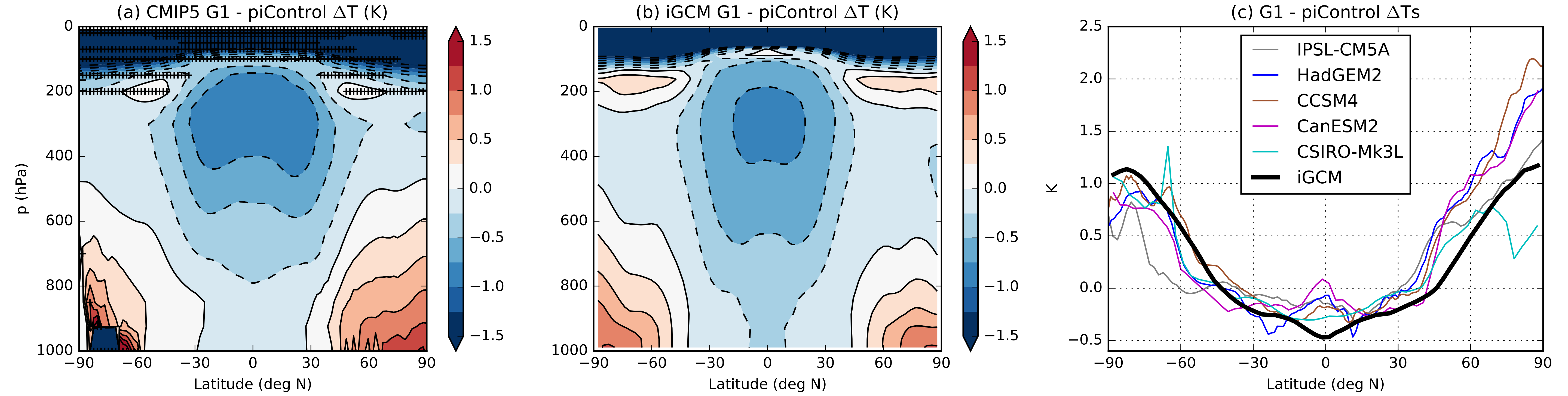

(a) CMIP5 G1 - piControl ΔT (K)
(b) iGCM G1 - piControl ΔT (K)
(c) G1 - piControl ΔTs
p (hPa)
Latitude (deg N)
K
IPSL-CM5A
HadGEM2
CCSM4
CanESM2
CSIRO-Mk3L
iGCM

fig2.eps.

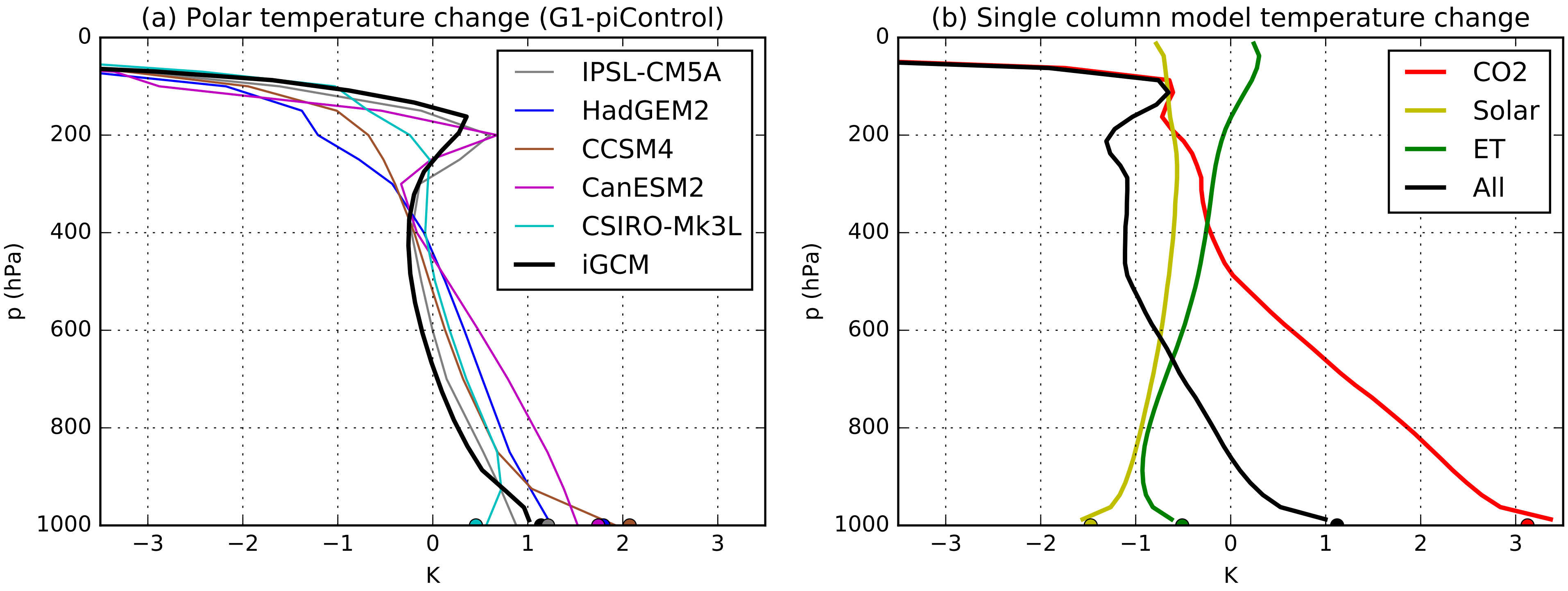
(a) Polar temperature change (G1-piControl)
p (hPa)
K
IPSL-CM5A
HadGEM2
CCSM4
CanESM2
CSIRO-Mk3L
iGCM
0
200
400
600
800
1000
−3
−2
−1
0
1
2
3
(b) Single column model temperature change
CO2
Solar
ET
All

fig3.eps.

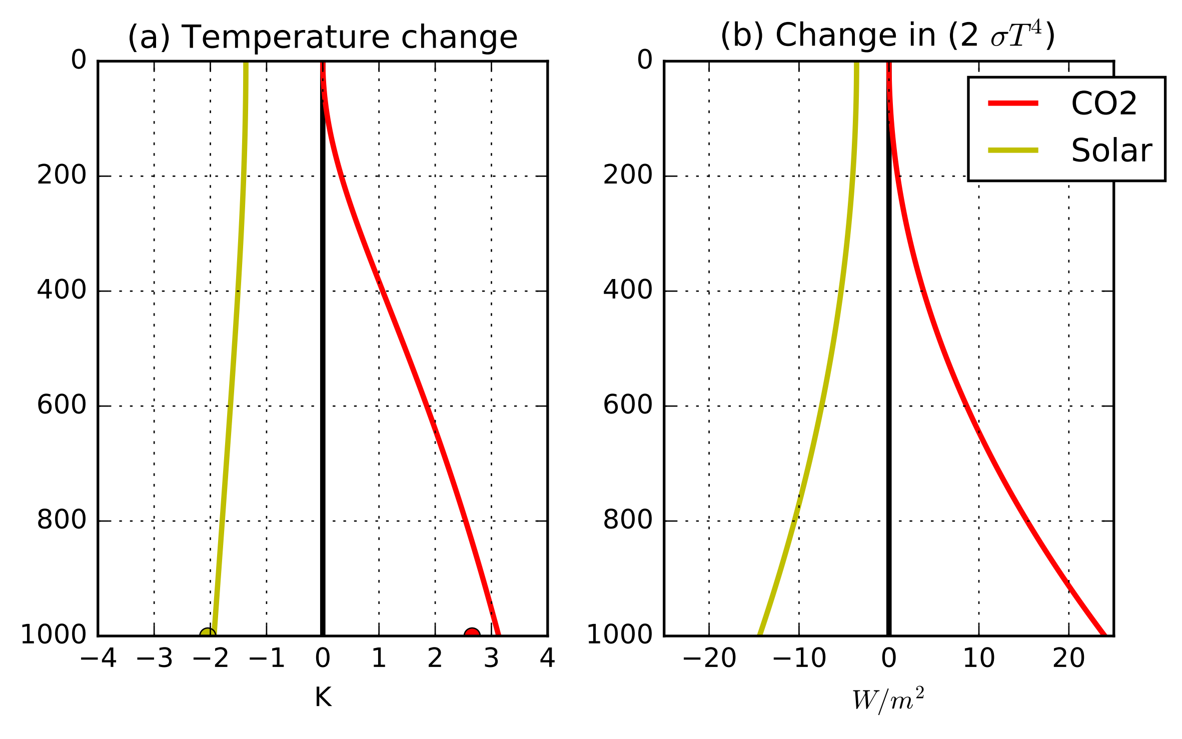
(a) Temperature change
0
200
400
600
800
1000
−4
−3
−2
−1
0
1
2
3
4
K
(b) Change in (2 σT^4)
0
200
400
600
800
1000
−20
−10
0
10
20
W/m^2
CO2
Solar